Advanced Industrial and Engineering Polymer Research 7 (2024) 201–214

Contents lists available at ScienceDirect

Advanced Industrial and Engineering Polymer Research

journal homepage: http://www.keaipublishing.com/aiepr

Full Length Article

# Bimodal impact strength distribution in HDPE composites: Formulational effects and Bayesian inference

David Viljoen [a, b], Johan Labuschagné [b], Ines Kuehnert [a, *]

[a] Polymer Processing Department, Leibniz-Institut fur Polymerforschung Dresden e.V., Hohe Str. 6, Dresden, 01069, Saxony, Germany
[b] Department of Chemical Engineering, Institute of Applied Materials, University of Pretoria, Lynnwood Rd, Pretoria, 0002, Gauteng, South Africa

ARTICLE INFO

*Article history:*
Received 30 May 2023
Received in revised form
6 October 2023
Accepted 8 November 2023

*Keywords:*
Bayesian inference
Polymer composites
Bimodal
Impact strength
Fractography

ABSTRACT

A bimodal impact strength distribution was found in notched impact specimens of HDPE composites with calcium carbonate, carbon black, SEBS and stabilisers. The bimodal distribution was only found at moderate-to-high calcium carbonate loadings, with the likelihood of low impact strength increasing with increasing stabiliser loading and decreasing with increasing SEBS/CB masterbatch loading. Bayesian methods were used first to confirm bimodality and then to investigate the effects of formulation on the performance of the system, based on a hierarchical model with quadratic and interactive terms and switching based on the sampling of a Bernoulli distribution with a logistic regression informing the probability of high or low impact strength. The results are contextualised through micrograph fractography and, briefly, differential scanning calorimetry. Results are also reported for unnotched impact tests, with negative correlations for impact strength with calcium carbonate and stabilisers, a positive correlation with SEBS/CB and interactive effects.



## 1. Introduction

Impact strength is a key specification of a product, as a measure of its resistance to rapid applications of force. As a result, impact strength is often the deciding factor in material selection [1]. Not only is the magnitude of the impact strength important, but, to guard against failure below specification, also its distribution. This is more important still in highly filled composites, owing to shifts in the ductile to brittle transition as a function of formulation [2,3].

These materials result from the use of a filler to augment the properties of a polymer matrix. One such matrix may be high-density polyethylene (HDPE), a widely used semi-crystalline commodity polymer with remarkable resistance to chemical attack [4], good impact strength [5] and the potential for exceptional weathering resistance with appropriate additives (as used, for example, in geomembranes [6]). Through the addition of calcium carbonate—a common filler—the stiffness, hardness and dimensional stability may be improved, typically at the cost of impact strength and tensile strength [7]. These losses may, however, be recovered or even reversed through careful material and loading specification, as well as surface modification [2,3,8].

HDPE is subject to auto-oxidative degradation, and thereby strongly benefits from the application of antioxidants. These compounds enhance material stability by deactivating radicals (primary antioxidants and hindered amine light stabilisers (HALS)) and reducing hydroperoxides to alcohols (secondary antioxidants) [4,7]. As a further stabiliser, carbon black is a highly effective absorber of UV radiation, converting it to heat, while also blocking its penetration into the material [7]. Carbon black is frequently introduced as part of a masterbatch, to counter health and safety risks associated with its fine-powder form as well as improving its dispersion and distribution through the matrix [9].

These additives not only affect the stability of the material, but may also cause changes in morphology or properties (such as impact or tensile strength). Further, these additives are known to show interactive effects in their impacts on material properties [10,11].

Bayesian inference is a method for statistical inference whereby a belief (prior) is updated according to data, resulting in a refinement of the belief (posterior). When paired with modern computational hardware and software, this method may be applied to parameter estimation in a similar way to that by which linear

* Corresponding author.
*E-mail addresses:* wd.viljoen@tuks.co.za (D. Viljoen), johan.labuschagne@up.ac.za (J. Labuschagné), kuehnert@ipfdd.de (I. Kuehnert).

https://doi.org/10.1016/j.aiepr.2023.11.001

regression may be used in Frequentist statistics. Further, as a result of the sampling methods utilised, more complex models may be utilised. These may include switching models [12], hierarchical models [13], or, more broadly, those making use of sampling from distributions. Support for heteroscedasticity may also be implemented directly in these types of models. The interested reader is directed to Kruschke's work [14] for a comparison of techniques as well as a detailed outline of the prior methodology.

This work reports on an unexpected apparent finding of the formulation-dependent presence of bimodal impact strength in notched specimens of composites of HDPE, calcium carbonate, masterbatched carbon black and a stabiliser package. Hereby, for some formulations, impact testing results suggested the presence of two clearly separated modes instead of the one expected for a material that is experiencing failure due to a consistent mechanism, only reported once elsewhere [15] to the knowledge of the authors. The proportion of specimens having high or low impact strength in the bimodal region would appear to be a function of formulation. These findings are first interrogated through a Bayesian statistical analysis to confirm bimodality, after which Bayesian hierarchical modelling is used to better understand the system and its behaviour in terms of the effects of the formulational parameters. The fracture behaviour of the system is characterised through microscope fractography to present additional physical context and evidence. Unnotched impact strength, transition temperature and crystallinity results are also reported, to better contextualise the performance of the materials.

## 2. Materials and methods

### 2.1. Materials

This study was performed based on commercially available materials, consisting of an injection-moulding grade of HDPE (Dow HDPE 25055 E, Midland, MI, USA); ultra-fine, surface-coated calcium carbonate (OMYA Hydrocarb® 95 T-OG, Oftringen, Switzerland); hindered amine light stabiliser (HALS)(Chimassorb 944, BASF, Rhineland-Palatinate, Germany); phosphite secondary antioxidant (Irgafos 168, BASF, Rhineland-Palatinate, Germany); and a carbon black masterbatch (Caparol NEFA MB F 21,504 Schwarz, Ober-Ramstadt, Germany). The HALS and secondary antioxidant were treated as a fixed stabiliser pack, at a 3:2 ratio. The carbon black masterbatch consists of 28 % of a furnace black (Orion Engineered Carbons Printex® F 80, Luxembourg), with an average particle size of 16 nm, in a thermoplastic elastomer (styrene-ethylene/butylene-styrene (SEBS) copolymer) matrix. The components will, henceforth, be referred to as HDPE, CC, S and CB.

### 2.2. Experimental design

This study follows on the work of Viljoen et al. [10,11] and makes use of the same experimental design. This design constrains the CC loading between 0 wt% and 60 wt% (36 vol%), that of CB between 0 % and 3.6 %, and that of S between 0 % and 0.5 %. For convenience, the materials will be referred to by a formulation shorthand: aCC/bCB/cS, where “a” is the percentage CC, “b” is the percentage CB and “c” is the percentage S. Two side-feed positions were trialled through the use of the validation formulation. The formulations used are enumerated in Table 1 and shown graphically in Fig. 1.

### 2.3. Processing

Compounding was performed on a KraussMaffei Berstorff ZE 25-Cl with a temperature ramp from 220 °C at the main feed to 235 °C at the die. Care was taken to configure an appropriate screw (1200 mm, 48D). HDPE, CB and S were introduced through the main feed, while CC was introduced through an earlier (14D) and/or later (25D) side feed. The extrudate was cooled in a water bath and pelletised.

Injection moulding was performed on an ARBURG 420 C, with a mould temperature of 50 °C and a barrel temperature profile of 40/210/200/210/220/230/230 °C. A linear injection flow rate of 40 mm/s was used with a peak injection pressure of 190 bar and a holding pressure of 78 bar.

Impact specimens were prepared in accordance with DIN EN ISO 179–2, with dimensions of 80 × 10 × 4 mm. A standard 2 mm notch was cut into the notched specimens, with a diameter of 0.5 mm.

### 2.4. Impact testing

Impact testing was performed on a Zorn Instruments (Stendal, Germany) Pendelschlagwerk at an impact speed of 2.9 m/s. All of the notched impact tests were performed using a 0.5 J pendulum, while unnotched tests were performed using a 4 J pendulum

**Table 1**
Experimental design: formulations and feed points. Reproduced with permission from Viljoen and Labuschagné, Polymer Testing; published by Elsevier, 2020 [10,11].

| | Component (%) | | | | CC feed | |
|---|---|---|---|---|---|---|
| Formulation | HDPE | CC | CB | S | 1 | 2 |
| 01 | 65.90 | 30 | 3.60 | 0.50 | | • |
| 02 | 65.90 | 30 | 3.60 | 0.50 | • | |
| 03 | 99.50 | 0 | 0 | 0.50 | | |
| 04 | 100.00 | 0 | 0 | 0 | | |
| 05 | 97.95 | 0 | 1.80 | 0.25 | | |
| 06 | 95.90 | 0 | 3.60 | 0.50 | | |
| 07 | 96.40 | 0 | 3.60 | 0 | | |
| 08 | 69.75 | 30 | 0 | 0.25 | | • |
| 09 | 67.70 | 30 | 1.80 | 0.50 | | • |
| 10 | 67.95 | 30 | 1.80 | 0.25 | | • |
| 11 | 67.95 | 30 | 1.80 | 0.25 | | • |
| 12 | 68.20 | 30 | 1.80 | 0 | | • |
| 13 | 66.15 | 30 | 3.60 | 0.25 | | • |
| 14 | 39.50 | 60 | 0.00 | 0.50 | • | • |
| 15 | 40.00 | 60 | 0 | 0 | • | • |
| 16 | 37.95 | 60 | 1.80 | 0.25 | • | • |
| 17 | 35.90 | 60 | 3.60 | 0.50 | • | • |
| 18 | 36.40 | 60 | 3.60 | 0.00 | • | • |

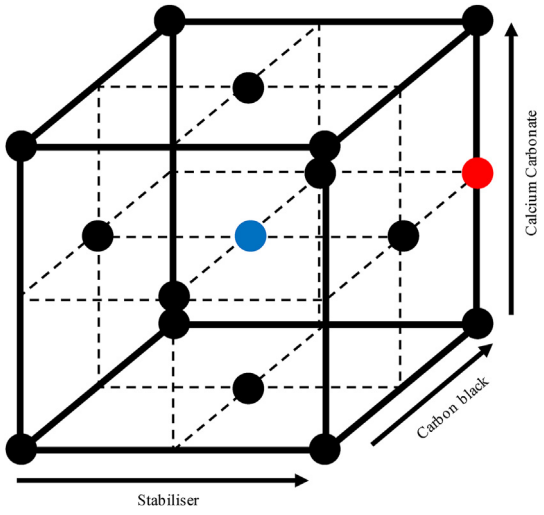


**Fig. 1.** Slack-variable representation of experimental design. Reproduced with permission from Viljoen and Labuschagné, Polymer Testing; published by Elsevier, 2020 [10,11].

(30CC) and 0.5 J pendulum (60CC). A WPM (Leipzig, Germany) PSd 50/15 was used with a 15 J pendulum in the characterisation of the 0CC unnotched specimens, owing to their high impact strength, but these results could not be used as the specimens were ejected from the machine without the initiation of fracture. Testing was conducted according at the standard climate (23 °C and 50 % humidity), and the specimens were allowed sufficient time to acclimatise.

### 2.5. Microscopy

Fractography was performed based on optical micrographs taken with a Keyence VHX-2000. Use was made of the stitching function, to allow for numerous (9 × 5) frames taken in a grid at 200x magnification to be combined into a final output for enhanced resolution. Use was also made of depth composition, wherewith the entire frame is produced in focus through an optical-focus sweep. This allows for small-scale fracture details to be investigated across a single micrograph, instead of requiring comparison across multiple images of different focal lengths. This does, however, come at the cost of the loss of broader topographic detail. The resulting micrographs were converted to black and white, with lightness minimised for white specimens and maximised for black specimens, in order to better represent fractographic detail. This was done in a standardised manner to avoid the introduction of bias.

### 2.6. Differential scanning calorimetry

DSC analyses were performed in a PerkinElmer DSC 4000, according to ASTM D3418 − 15 [16], making use of open aluminium pans under a nitrogen atmosphere (with a 20 ml/min flow rate). Granules were used directly for the measurement, with a mean weight of 13.0 mg. Preliminary thermal cycles were performed, with the specimens heated to 180 °C at 10 °C/min and held there for 5 min. The cooling curves were then recorded, with cooling to 30 °C at 10 °C/min. After the specimens were held at 30 °C for 5 min, the heating curves were recorded with heating to 180 °C at 10 °C/min.

### 2.7. Statistical analysis

Slack-variable representations with standardised variables are used instead of conventional mixing models such as Scheffé polynomials for the sake of more readily interpretable parameters, with HDPE loading taken as the slack variable. Note that the dependent variables were not standardised, to give the reader more contextual understanding on the size of the effects.

Standardisation was chosen over normalisation as it centres the model nearer the centroid of Fig. 1. This allows the models to better reflect the switching behaviour, by placing the reference point in the region where switching may occur. Normalisation would centre the model on the virgin material, which was found to have deleterious effects on the quality of fit. Despite this, the effects seen using standardisation and normalisation are, broadly, similar.

Inference was performed using the PyMC3 [17] framework on Python 3.6, using 4 threads. 10,000 samples and 20,000 tuning samples were drawn per thread. Some hyperparameter optimisation was performed to settle on these values, with the goal of smooth and consistent posterior parameter distributions and no divergences. Throughout, different uninformative priors centred on the null values were trialled, with no clear distinction between the resulting posteriors. Sampling was performed using no-U-turn sampling (NUTS) [18], a derivative of Hamiltonian Monte Carlo sampling, for its efficiency and insensitivity to correlated parameters (present owing to the interaction and square terms). Conventional measures used in Frequentist inference, such as $R^2$, are not necessarily suitable to Bayesian regression. While Bayesian $R^2$ is available in the literature, it is not indicative of the quality of fit to a fixed target (input data) but rather a measure of the proportion of explained variance for new (predicted) data [19]. As a result, it is omitted in preference of investigation of the posterior predictive fit and the correlation between observed and predicted data through goodness-of-fit plots.

To guard against false positives, regions of practical equivalence (ROPE) are established [20]. Much of the related literature is found in observational science, stemming from social science, psychology and similar fields. Therefore, some changes are brought as the data here are based on a experimental set of independent variables, with similar likelihoods of being distributed at the low, medium and high levels, and increased sensitivity to changes in the dependent variable is sought due to investigatory nature of the work. As a result, ROPE for parameters are assigned to a change in the dependent variable of 1 % of the range of the dependent variable over the full range of the pertinent independent variable in the linear equations. Similarly, ROPE are assigned to a 5 % change in likelihood of the logistic function. Here, the ROPE are used not as hard boundaries but as aids to analysis, coupled to the region of the 95 % highest-density interval (HDI). If the HDI is entirely within the ROPE, is is likely that the effect of the parameter is a null value, here indicative of no or a very weak effect. If the HDI is entirely outside the ROPE, it is likely that the effect of the parameter is significant, while overlapping HDI and ROPE boundaries are indicative of uncertain parameter effects that would require additional experimental data points for findings to be made. It must be noted that the ROPE criteria are set fairly low, as this is merely an exploratory work. For practical formulational work and decision making, it may be advisable to use more aggressive limits, such as a 5 % or higher change for parameters in the linear equations.

All relevant fitted parameters, standard deviations and goodness-of-fit plots are presented in Appendix A, with key figures mentioned in the text.

## 3. Results

### 3.1. Notched impact strength and bimodality

The notched impact results are presented in Fig. 2. From here, it can clearly be seen that there is a decline in impact strength with

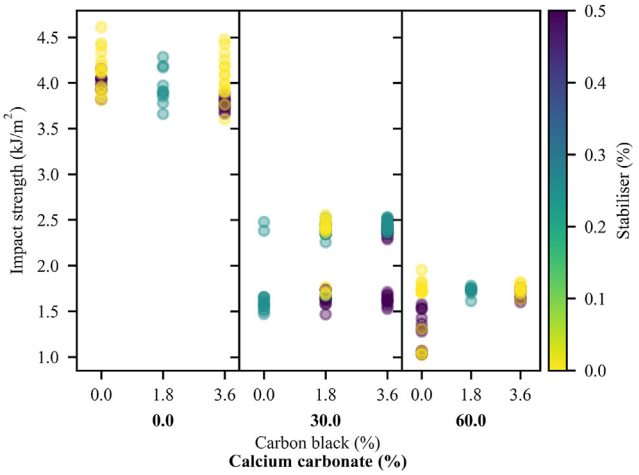


**Fig. 2.** Raw data for the notched impact strength of the composites. Note, here, the distinct bimodal appearance in the 30 CC materials as well as the general negative trend with increasing CC loading.

increasing CC, moving towards what appears to be a plateau. The systems appears to exhibit bimodal behaviour in the 30CC region and, potentially, the 60CC/0CB region. To further motivate this, a statistical check may be used. However, the standard methods to discern between unimodal and bi/multimodal data are incompatible with the full data here. Hartigan and Hartigan's Dip Test for Unimodality [21], the bimodality coefficient [22] and several other techniques are only compatible with univariate data [23]. This is a problem as, for example, data generated by a linear relationship between dependent and independent variable could appear multimodal if there are only few (but multiple) steps in the independent variable (as are present here). Siffer et al.'s [23] Folding Test of Unimodality is compatible with multivariate data, but, again, will suggest multimodality in a system with few steps in the independent variables. Akaike's information criterion used with one- and two-component Gaussian mixture models, tends to suggest bimodality in most cases [24]. However, tailoring the model to use one or two linear equations (of the form given in Equation (1)) and assessing the quality of fit as well as the standard deviation of the system may prove fruitful.

$$\hat{\mu} = c_0 + \sum_{i=1}^{n}\left(c_i x_i + \sum_{j=i+1}^{n} c_{i;j} x_i x_j\right) \tag{1}$$

Model goodness for Bayesian models may be estimated using posterior predictive accuracy, with the two leading approaches being leave-one-out cross-validation (LOO) [25] and the widely applicable information criterion (WAIC) [26]. Despite the approaches being asymptotically equal, some controversy exists over which is superior—based on arguments over robustness [25] and bias [27]. For simplicity, both are used in this study. It should be noted that both approaches penalise model complexity to allow for increased fairness in comparison. Here, the LOO for the unimodal model is −32 and the LOO for the bimodal model is 165, with the same values for the WAIC—with higher values indicating increased accuracy. This shows the substantial superiority of the bimodal model based on LOO and WAIC, and may be further motivated with the mean standard deviation for the unimodal model (0.31 kJ/m$^2$, Figure A2) being more than five times that of the bimodal model (0.057 kJ/m$^2$, Figure A5). Finally, using the posterior parameters, it is possible to estimate a distribution of the difference between the high and low levels in the bimodal model (Fig. 3), with a mean of 0.74 kJ/m$^2$. Here, the ROPE is set to a change of three standard deviations (taken as the mean standard deviation of the model) around zero.

Dependence on the formulation was found in the high- and low-impact-strength subsets (Figure A3 and Figure A4, Appendix A), albeit with only very weak effects. Here, the ROPEs were defined on the impact-strength range of the complete 30CC set, thus including the higher and lower impact strengths. In the case of the higher impact strength, a negative correlation (−25 J/m$^2$) was found with S loading with the other parameters undecided. In the lower-impact-strength subset, a negative effect (−45 J/m$^2$) with S, a positive effect (45 J/m$^2$) with CB and an antagonism (−44 J/m$^2$) between CB and S were found.

The correlation between formulation and the likelihood of high/low impact strength in the 30CC region was determined as a function of the loadings of CB and S, and their interaction. This was done by comparing a Bernoulli distribution with its probability of a high value given by the posterior of a Bayesian logistic regression (of the form given in Equation (2), with an uninformative prior), with a Bernoulli distribution with a constant probability (with a prior given by the fraction of high values in the subset (67 %), for maximum accuracy). Here, the logistic model outperforms the simple model with the LOO and WAIC of the logistic model −58 compared to the −75 of the simple model. The mean function (equivalent to the least-squares fit) of the logistic model is plotted in Fig. 4. Inspection of the posterior parameters (Figure A6 and Figure A7, Appendix A) also conveys confidence in the result. Most notably, there is a direct correlation between the S loading and the likelihood of lower impact strength and between the CB loading and the likelihood of higher impact strength. Antagonism was suggested between the parameters, but there is a slight overlap of the HDI and the ROPE—leaving this effect undecided.

$$\hat{p} = \left(1 + e^{-\left(c_0 + \sum_{i=1}^{n}\left(c_i x_i + \sum_{j=i+1}^{n} c_{i;j} x_i x_j\right)\right)}\right)^{-1} \tag{2}$$

Several hypotheses could support the results observed. Owing to this uncertainty, the combined model is structured to best reflect the experimental data and the trends observed as a function of formulation, while being structured to be as general as possible and avoiding extrapolation from experimental results under the hypothesis of at least two failure modes. The model is updated in a tiered fashion. Linear models (of the form given in Equation (3)) were introduced with uninformative priors for the higher and lower impact strength cases. The priors for the higher impact strength are updated on the subset of all data except that where

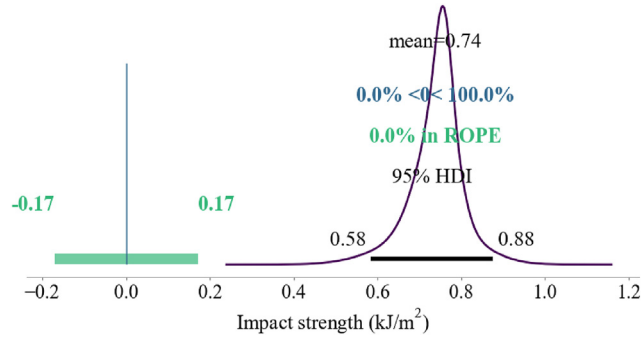


**Fig. 3.** Posterior parameter distribution for the difference between high and low levels in the bimodal model of the 30CC materials.

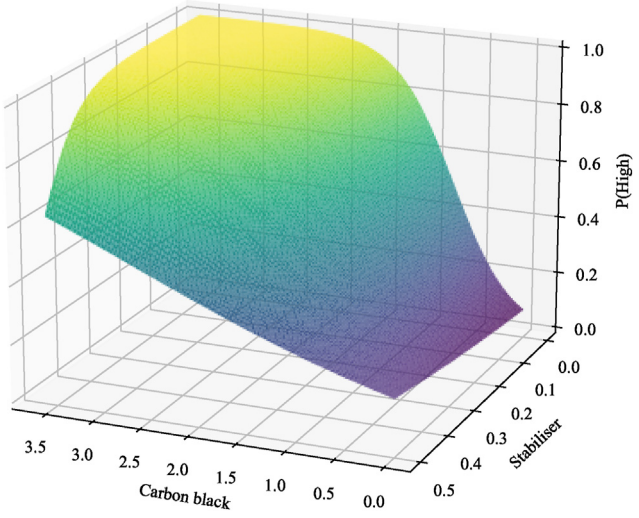


**Fig. 4.** Surface plot of the mean of the posterior of the Bayesian logistic regression on the likelihood of high impact strength as a function of formulation.

fractography and impact results support a lower value. The same is done for the priors for the lower impact strength, in updating on all data except where fractography and impact results support a higher value. The posteriors that result are used as priors for these equations in the full model. Switching between these models takes place based on the sampling of a Bernoulli distribution taking a logistic regression (of the form given in Equation (4)) as probability. This switching section is initialised with uninformative priors within the complete model, with its updating based on a Boolean variable indicating high or low impact strength for a given specimen.

$$\hat{\mu} = c_0 + \sum_{i=1}^{n}\left(c_i x_i + \sum_{j=i}^{n} c_{i,j} x_i x_j\right) \tag{3}$$

$$\hat{p} = \left(1 + e^{-\left(c_0 + \sum_{i=1}^{n}\left(c_i x_i + \sum_{j=i}^{n} c_{i,j} x_i x_j\right)\right)}\right)^{-1} \tag{4}$$

The combined model (Equation (5)) switches output between the higher and lower linear models as a function of sampling from the logistic-model-informed Bernoulli distribution. Owing to fairly substantial heteroscedasticity, the standard deviation of the system was taken as a linear function (Equation (6)) of the output of Equation (5). Uncertainty in the response variable, then, can be incorporated through sampling from a normal distribution taking Equation (5) as mean and Equation (6) as standard deviation as shown in Equation (7). This approach not only allows for inference of the means and distributions of samples, but also for the estimation of the likelihood of a sample to come from a given (high/low) distribution. The model is elucidated as a flow chart in Fig. 5. The authors were unable to find a model of this type in the literature, but it is conceptually close to the Bayesian Markov-switching models that are applied to sequential data in econometrics [12] and epidemiology [28], among other fields, differing in terms of the intent and mechanism of switching.

$$\hat{\mu}_{full} = \hat{\mu}_a + \mathrm{B}(1, \hat{p})(\hat{\mu}_b - \hat{\mu}_a) \tag{5}$$

$$\sigma = c_0 + c_1 \hat{\mu}_{full} \tag{6}$$

$$\hat{y} \sim \mathcal{N}(\hat{\mu}_{full}, \sigma) \tag{7}$$

In the numerous cases where inconclusive evidence exists for high or low impact strength for a given specimen, two methods were trialled: (1) consider all of inconclusive cases, along with the higher impact strength cases, as the “high” state (Boolean 0) with the lower impact strengths as a “low” (Boolean 1), or (2) randomly assign inconclusive cases to “high” or “low” states with equal odds. The latter method was found to be unsuccessful, as the logistic function's output tended towards a constant for all formulations. Therefore, the prior approach is chosen.

Upon completion of the inference, the model offers a mean posterior predictive fit of the notched impact strength as shown in Fig. 6a. If noise is included, the posterior predictive fit shown in Fig. 6b results. The posterior parameter distributions are presented in Figure A12 to Figure A15 in Appendix A.

If Fig. 6b is compared to Fig. 2, it is clear that the experimental data are well described by the Bayesian model. Numerically, adequate convergence is indicated by a rank-normalised of no more than 1.001, indicating similar variance between and within chains. Further, stability is indicated by effective sampling sizes (ESS) of the order of $10^4$. This relates to the (autocorrelation-corrected) number of points in the sampling chain [29,30].

The similarity of the parameters for high and low impact strength may be noted though investigation of the posteriors parameter distributions, Figure A13 and Figure A14. The strongest effect by far (around $-0.85$ kJ/m$^2$) is the negative correlation with CC. A weakly positive effect (0.08 kJ/m$^2$) is associated with increasing CB in the weaker class of specimens, while CB has little effect in the stronger class of materials. Weakly negative correlations (around $-0.07$ kJ/m$^2$) are seen with S. A weak (lower, 0.12 kJ/m$^2$) to very weak (higher, 0.03 kJ/m$^2$) synergy between CC and CB can be seen, while a very weak (0.03 kJ/m$^2$) synergy can also be seen between CB and S in the stronger specimens. A medium (higher, 0.23 kJ/m$^2$) to strong (lower, 0.57 kJ/m$^2$) positive correlation exists with the squared CC term, relating to the convex curvature observed with increasing CC. In the weaker specimens, weakly negative ($-0.08$ kJ/m$^2$ and 0.09 kJ/m$^2$) correlations can be seen with the squared terms for CB and S.

The heteroscedasticity of the system is approximated through a linear equation, which yields evidence that the error consists of a small fixed component (with a mode of approximately 0.01 kJ/mm$^2$) and a component that is a function of the IS (at about 3.7 % of IS).

Strikingly, it can be seen from Fig. 7 that there are very strong formulation effects on the likelihood of high/low mode in the bimodal region, and that the logistic function is performing as expected on the unimodal subsets with high values for p (High). It is clear that CB increases the likelihood of a high-strength fracture, with a moderate positive effect (2.8 (1)), while S has a weakly negative effect ($-1.6$ (1)). The increased likelihood of a low-strength fracture in the middle of the CC range is provided by a strong positive effect (11 (1)) for the quadratic CC term, setting the stage for the sensitivity of the system to the CB and S loadings seen in the 30CC materials, while a weakly negative effect ($-1.8$ (1)) is present for the quadratic S term. Owing to the wide variance of the effects, the remainder are undecided—with HDIs frequently overlapping not only the ROPE but also the null value.

### 3.2. Unnotched impact strength

It was not possible to determine the impact strength of the unnotched specimens of the 0CC materials, as the specimens did not fracture before being ejected from the test position as a result of the impact. A lower limit on their impact strength can be estimated, however, as the ejection tended to occur at around 6 J of energy dissipated through impact. This corresponds to an impact strength of at least 150 kJ/m$^2$ under the test conditions. Of course, some losses may be associated with the ejection process, so these values should only be considered as rough estimates. The 30CC and 60CC materials could, however, be characterised in this manner (Fig. 8a).

A strong decrease in impact strength is seen with an increase in CC from 30 wt% to 60 wt%. This is coupled to a moderate positive correlation between CB loading and impact strength in the 30CC cases, with this effect almost entirely vanishing in the 60CC cases. Throughout, there is evidence for the moderate negative impact of S on the impact strength of the system. These findings are echoed by the posterior-predictive and posterior-parameter distributions (Fig. 8b and Figure A19, Appendix A). A strong negative correlation ($-12$ kJ/m$^2$) is found with CC, and weak-to-moderate effects for CB (2.2 kJ/m$^2$) and S ($-1.6$ kJ/m$^2$). The diminished effect of CB at the 60CC loading is shown through a moderate-to-weak $-1.7$ kJ/m$^2$ antagonism between CB and CC. Interestingly, a weak synergy (0.97 kJ/m$^2$) is found between CC and S, pointing towards a reduction in negative correlation between impact strength and S with increasing CC. To accommodate the reduced number of points in the independent variables, owing to the failed 0CC tests, the model used is of the form given in Equation (1), again with standard

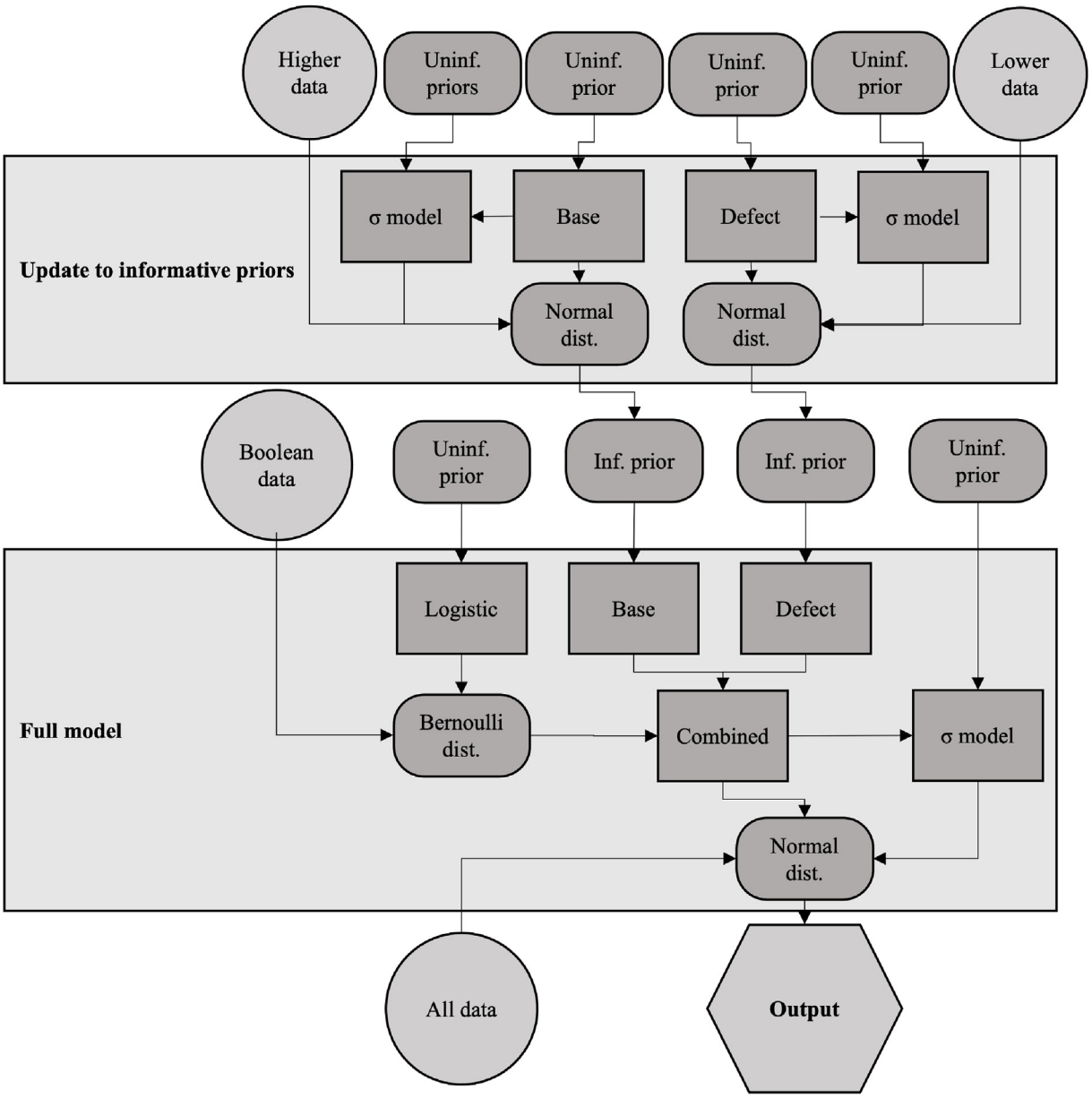


**Fig. 5.** Flow chart of the model structure and updating methodology.

deviation a linear function of the mean of the dependent variable. The fixed component of the standard deviation is centred on 0 kJ/m$^2$, with a tail stretching to 0.1 kJ/mm$^2$, while the variable component is centred on 11 % of impact strength.

### 3.3. Fractography

To better contextualise the effects of formulation on performance, it may be beneficial to gain a better understanding of the mechanisms involved in fracture—particularly regarding the bimodal notched impact strength. To this end, fractography of some relevant specimens may offer insights into the type and progression of fracture through the specimens. Interestingly, the sound of the fracture could be qualitatively correlated with the impact strength, as the stronger specimens had a sharper sound of failure than that of the weaker specimens. Fractography is performed based on a number of preceding works [31,32], noting particularly the works by Böhning, Niebergall et al. [33–35]. The works by Mishra et al. [36–38] are omitted from this discussion, due to incompatibilities between these works and those of Böhning, Niebergall et al. in terms of the discussion of the near-impact-edge fracture morphology, and the better fit of the works of Böhning, Niebergall et al. with the results here observed.

First, comparisons may be drawn between specimens of the same formulation (3.6CB/30CC/0.5S) that exhibited high and low impact strength. These are shown in Fig. 9a (high) and Fig. 9b (low). These are virtually identical to the corresponding fracture surfaces of the other 30CC specimens that contain CB—to the point that high or low impact strength can be determined from the fracture surface alone in all cases. The manner of crack propagation seems to differ somewhat between these specimens. It is clear in all cases that fracture was initiated on the notched edge, with predominantly brittle failure. Moving further away from this edge, to the so-called “mirror zone” [31] directly adjacent to the origin and identifiable by

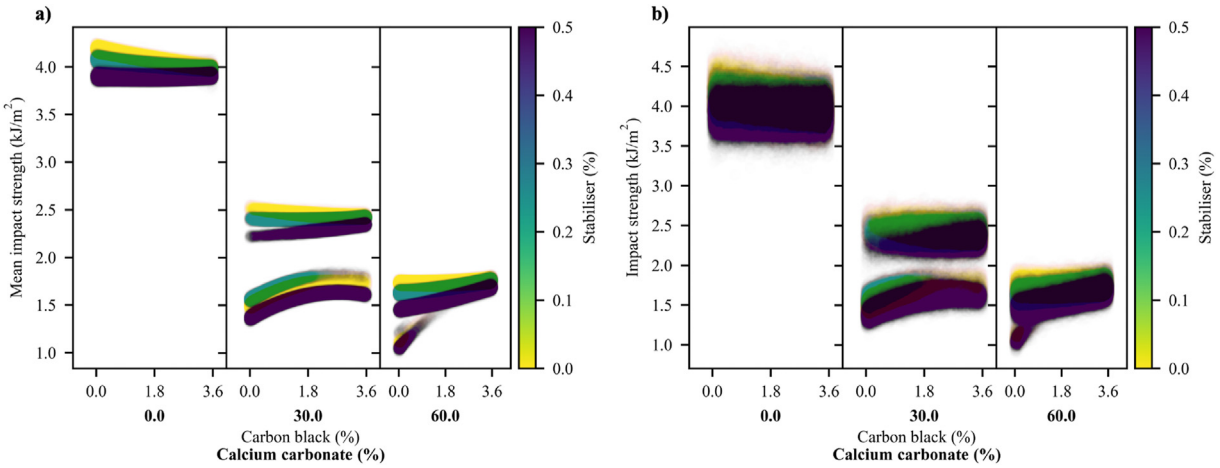


**Fig. 6.** Plot of the mean (a) and randomly sampled (b) posterior predictive fit of the Bayesian regression for the notched impact strength as a function to the formulational variables.

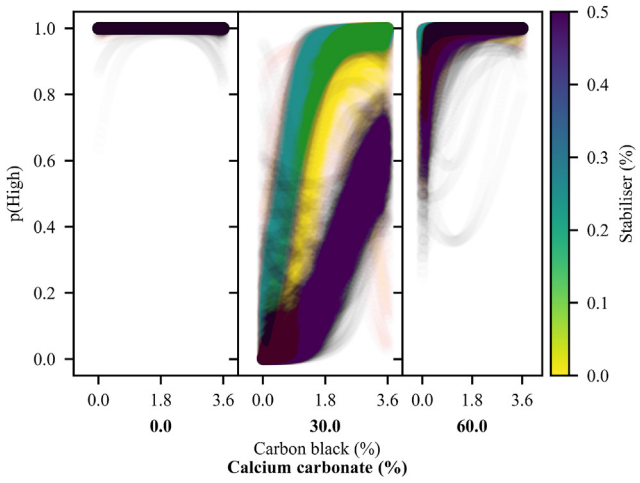


**Fig. 7.** Plot of the posterior probability of high-state failure as function to the formulational variables.

its lighter colour, it is clear that the initial fracture spread more evenly and substantially from the origin at its centre in the case of the stronger specimen—indicated by the larger and more smoothly elliptical area. This is opposed to the much smaller and more uneven mirror zone in the weaker specimen, which may suggest multiple fracture origins and rapid progression past this mode of failure. This zone is typically seen as the remnant of a ruptured craze [31], as can be deduced from the lighter colour, which would be brought on by the remnants of the craze fibrils, and thus as a more ductile form of failure than that seen in the large and smoother brittle-failure regions. The larger mirror zone in the stronger specimen would suggest more impact energy being dissipated in this mode of failure. This region can be seen to smoothly transition from extensive fibrillation (in the lightest part of the region) to very little fibrillation in the brittle region. The first brittle region is of approximately the same size between the specimens. In this region, it must be noted that local areas of more ductile or more brittle fracture exist, based on the rougher or smoother topography of the surface. Following this, a rib marking (also referred to as a "crack arrest marking") can be seen—possessing morphology similar to that first seen in the mirror zone—indicating a region where the rate of crack progression slowed substantially. The transition to this region is much more abrupt in the case of the weaker specimen. Further, the morphology of these regions differ slightly between the specimens. In the weaker specimen, the fracture morphology closely resembles the that of the near-notch mirror zone, while the fracture

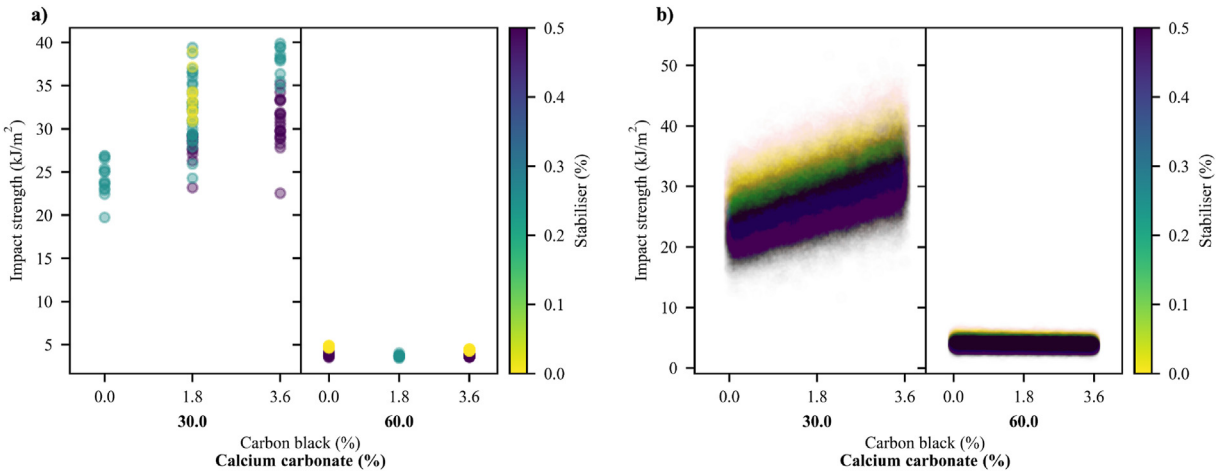


**Fig. 8.** (a) Raw data for the unnotched impact strength of the composites; (b) model prediction with noise. Note, here, the negative impact of increasing CC loading, the positive effects of CB at the lower CC loading and the significant heteroscedasticity.

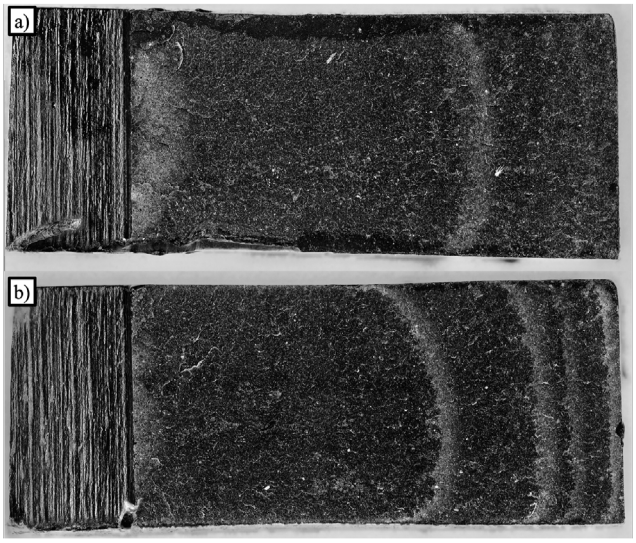


**Fig. 9.** Micrographs of fracture surfaces of 3.6CB/30CC/0.5S: (a) high impact strength; (b) low impact strength.

morphology of the rib marking in the stronger specimen more closely resembles that of the near-brittle zone of the mirror zone. Another brittle region follows this, interrupted by two further clear rib markings in the weaker specimen and two ill-defined rib markings to the impact edge in the stronger specimen. These latter rib markings can be seen to flatten out and lose contrast as they approach the impact edge. The increased number of rib markings in the weaker specimens point toward the earlier failure of these specimens, as a reduced angle between the fracture planes would offer a reduced rate of extension—offering more chance for fibrillation to take place. Finally, the weaker specimen exhibits a significantly whitened region up to the impact edge of the specimen. Based on the works of Böhning, Niebergall and others [33–35], this can be attributed to a compression region resulting from the rotation of the two sides of the fracturing impact specimen around the pivot points that are the limits of the specimen holder.

If attention is paid to the long edges of the specimens, it can be seen that some smooth regions exist. The authors believe that these may be linked to folded-in sections of the skin layer that have deformed plastically. Far larger areas of this may be seen in the stronger specimen than in the weaker specimen. By visual inspection, large/deep regions of tearing may be seen in the origin/mirror zones of the stronger specimen. In contrast, the weaker specimens have relatively flat profiles across their failure surfaces. In summary, then, it would appear as though the stronger specimens resisted the early phase of fracture more substantially, through significant void formation and elongation across multiple planes, with a rapid and high energy failure following the failure of the fibrils resulting from the crazes. In contrast, little resistance to fracture was initially offered by the weaker specimens, with the more brittle fracture allowing numerous stick-slip regions through the slowing of the fracture front. These, likely, had less of an effect on the strength of the specimen, owing to their closer proximity to the fulcrum which is the impact edge and the effects that this has on the internal stress state.

Next, the 60CC materials containing CB may be investigated using the same approach. The micrographs are presented in Fig. 10. Overwhelmingly, the fracture surfaces appear internally consistent, suggesting consistency in terms of the failure mode—in agreement with the impact-testing results. The surfaces and strengths are also

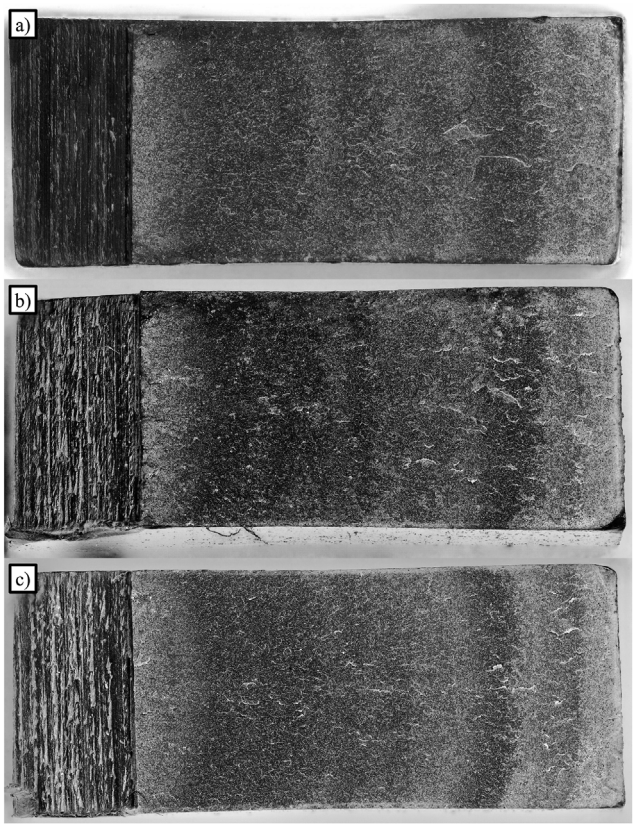


**Fig. 10.** Micrographs of fracture surfaces of the 60CC specimens with CB: (a) 1.8CB/60CC/0.25S; (b) 3.6CB/60CC/0.5S; (c) 3.6CB/60CC/0S.

similar to those of the weaker 30CC specimens. A notable difference, however, lies in the increased propensity and size of fine ledges in the 30CC specimens—with these originating from intersecting fracture planes. Rib markings are much more common in these materials, akin to what is seen in the weaker 30CC specimens. At the same time, these specimens offer relatively smooth topologies across the board. The mirror zones of these materials have much reduced curvature compared to those of the stronger 30CC specimens, likely pointing to faster crack propagation past these zones and modes. The mirror zone in the 3.6CB/60CC/0S specimens appears to be slightly larger and more regular than those of the 1.8CB/60CC/0.25S and 3.6CB/60CC/0.5S specimens. Increasing in scale towards the impact edge, some elongated while features can be seen. These appear to be connected to ledge-like features, suggesting the progressive slowing of the fracture front to the point where areas subject to intersecting fracture planes can exhibit fibrillation. A number of faint rib markings can be seen along the fracture path, culminating in a large area near the impact edge with increasing whiteness nearing the edge. This would appear to be the compression region. The extreme whitening right on the impact edge would suggest the presence of a hinge in each of the cases. This would suggest that the fracture front is slowing as it is approaching the impact edge, allowing for more extensive crazing to occur, likely coupled to the compression zone. The hinge, of course, would then be subject to the slowest fracture in a given specimen, resulting in its extensive whitening. It is, further, interesting to note the distinct skin layers that can be seen on the long edges in all three cases, either as extremely flat/brittle failure areas or as more uneven, whitened areas. In the 3.6CB/60CC/0S specimen, however, these skin layers appear to have much more consistent crazing on their surfaces. This whitening is thought to result from

"shear lips", where the edges of the specimen fail at an angle to the fracture plane (approximately 45°). This is frequently seen in the fractography of metals [39], and has been reported by several authors in HDPE-containing systems [33–35].

Finally, the fracture surface of a representative specimen of the 0CC materials containing CB may be investigated—shown in Fig. 11 for the 1.8CB/0CC/0.5S material. The fracture origin can now be seen more clearly at the base of the mirror zone, while the mirror zone itself is much smaller than it was in the prior examples. The zone following the mirror zone is much rougher than seen in the prior examples, suggesting more ductile failure, and it appears to become progressively more ductile further from the notch. This is interrupted by a partial rib region, after which there is a return the relatively ductile failure. Around this region can be seen a curved area with significant whitening, which the authors believe to be a variant on the typical compression region—having the fracture progress through the centre while the sides have slowed fracture due to their compression and, potentially, the effects of the increased molecular orientation near the walls of the mould. This, again, ends in a slightly more whitened area on the impact edge, believed to be the remnant of the hinge. Skin layers can clearly be identified on the long edges, exhibiting little evidence of micro voids and fibrillation on the edge. Once past these regions, these fine features can be seen. In addition, there is evidence of shear lips on the edges starting on the notched edge, giving credence to the much more ductile failure of these types of specimens as can be seen from their increased impact strength.

In the case of the materials without CB, insufficient contrast was available to allow analysis by micrograph fractography. Some findings could be made by visual inspection. In the 0CB/30CC/0.25S material, it may first be seen that the stronger specimens exhibit morphology corresponding to a more ductile failure on the notched edge, with smoother macro features reminiscent of tearing and extension (with the accompanying whitening), while the weaker specimens exhibit more jagged features that may be associated with a rapid crack progression. The specimens exhibit the same characteristic rib markings as seen in the 30CC specimens with CB, the first of which is the most distinct, with more numerous rib markings in the case of the weaker specimens. Finally, the weaker specimens exhibit a distinct transition into a smoother surface extending to the impact edge, again similar to what is seen in the 30CC specimens with CB.

As can be seen in Fig. 2, a tight cluster of low impact strength results is accompanied by a more distributed grouping of stronger results for the 0CB/60CC/0.5S material. By visual inspection, it can be seen that the weakest of the results suffered a very brittle and planar failure, with smooth edges. This is in contrast to the strongest specimens of the upper cluster, where distinct unevenness and even tearing can be seen on the notched edge, while a more prominent compression zone and/or hinge can be seen on the impact edge. It is difficult to assess the number of rib markings in these specimens, owing to the low contrast. In the 0CB/60CC/0S material, distinct whitening reminiscent of fibrillation can be seen on the long edges of the stronger specimens—absent in the weaker specimens. Specifically, these regions appear within the skin layer. The weaker specimens of the upper cluster exhibit a mix of the prior results, with some unevenness in the notched edge, but, in general, a more planar surface. This would suggest that there is continuity in the failure mechanisms for these formulation regions.

**Fig. 11.** Micrographs of fracture surfaces of the 0CC/1.8CB/0.25S specimen.

### 3.4. Crystallinity

A check on the crystallinity of the materials may prove valuable, as the nucleation conditions vary widely between the different formulations. The raw data are presented as percentage crystallinity of the composite (Fig. 12a), to illustrate the effect of the replacement of HDPE with the other additives) and as an approximation of the HDPE crystallinity alone, correcting for loading (Fig. 12b). Shown in the figures are the crystallinities calculated from the crystallisation and melting enthalpies, where it can be seen that the crystallinity calculated based on the enthalpy of melting exceeds that based on the enthalpy of crystallisation for the 0CC specimens. The opposite is true for 60CC specimens, while the effect is somewhat mixed for the 30CC specimens—skewing towards higher crystallinity based on the melting enthalpy. With reference to Fig. 12b, it can be seen in the 0CB/0CC cases that the presence of the stabiliser slightly suppresses crystallisation. In the presence of CC, this becomes more complicated—with the crystallinities of the 0CB/60CC/0S specimens somewhat suppressed compared to those of the 0CB/60CC/0.5S specimens. Bayesian inference based on equations of the form of Equation (3) shows that few parameters carry high significance (the parameters are presented in Figure A23 to Figure A25), as may be expected from the complex effects in Fig. 12. CC has a strong negative primary effect on the composite, while no clear effects are found in the HDPE crystallinity data, with only a weak antagonism between CB and S suggested but left uncertain due to slight overlap with the ROPE. Based on the complex curvature of the results, it is likely that higher-order effects are present.

A similar pattern may be observed in the melting and crystallisation temperatures (Fig. 13), with no clear effects identified through Bayesian inference. However, it is interesting to note that the virgin material has the highest melting temperature and lowest crystallisation temperature of all. In terms of single-change effects, the addition of CB, CC and S each has a negative effect on melting temperature and a positive effect on crystallisation temperature.

An investigation of the melting difference curves [40], shown in Fig. 14, generally reveals the expected increase in the proportion of smaller crystallites and the accompanying decrease in larger crystallites with increasing additive loading. This can be seen by the appearance of a peak followed by a trough as time (and temperature) increases. In addition, the peaks exhibit long tails to the left, suggesting the presence of much smaller crystallites. These peaks are constructed by subtracting the melting curve of the virgin material from that of the composites, with the weights of HDPE having been standardised across the measurements. Throughout, a trend towards a proportionally increasing tail of small crystallites can be seen with increasing CC, as well as a skewing of the ratio of change in smaller/larger proportion—suggesting that while an increase in CC results in an increase in the proportion of smaller crystallites, it results in a more substantial decrease in the proportion of large crystallites. Finally, it would appear that the number of smaller crystallites passes through a peak at a CC loading of around 30 %. Paying attention to Fig. 14a, it can be seen that 0CB/30CC/1.8S exhibits a particularly strong increase in the number of smaller crystallites, while 0CB/0CC/0.5S curiously exhibits

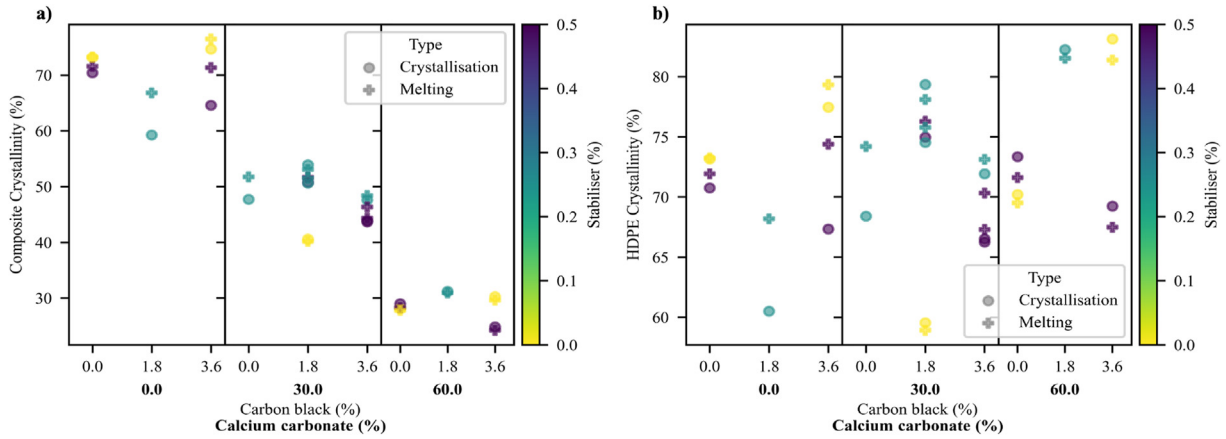


**Fig. 12.** Plot of the composite crystallinity (a) and estimated matrix crystallinity (b) of the materials as a function to the formulational variables.

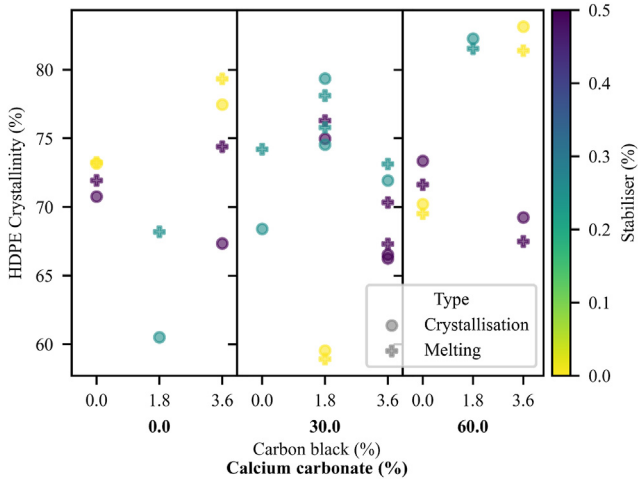


**Fig. 13.** Plot of the melting and crystallisation temperatures of the materials as a function to the formulational variables.

decreases in the proportion of smaller and larger crystallites, countered by an increase in mid-sized crystallites. In Fig. 14b, it is most notable that 1.8CB/30CC/0S exhibits a minor increase in smaller crystallites, countered by a significant decrease in larger crystallites. In Fig. 14c and d, duplicated formulations reveal small to moderate variance in results. A reduction in deviation from the crystalline structure of the virgin material can be seen with increasing CB for the 30CC materials in Fig. 14d.

## 4. Discussion

It is clear, first, that multiple fracture modes exist—based on fractography. Based on statistical analysis, it may also be seen that bimodal impact strength as a function of formulation is present in the notched specimens. Further, it is found that the proportion of high/low impact strength in the bimodal area is a function of formulation. The only prior literature that the authors could find reporting bimodal impact strength in polymers relates to an investigation of the ductile-to-brittle transition temperature of PVC [15]. There, impact-modified PVC plates were found to exhibit bimodal (falling-dart) impact strength near their ductile-to-brittle transition, with the probability of more ductile failure increasing with increasing temperature. A notable difference between that work and the present is that the results in the present work are much nearer to the modes, with no points in the intermediate region.

This bimodality is in contrast to the typical behaviour of polymers according to the Ludwig-Davidenkov-Orowan hypothesis, where the ductile to brittle transition is expected to occur when the yield stress exceeds a critical value—with brittle fracture and plastic flow taken as distinct processes [41,42]. Specifically, the critical value is the point at which the flow (ductile) stress would exceed the fracture (brittle) stress; naturally with the yield stress always being the lowest of the two stresses. Given the sensitivity of plastic flow, particularly, to temperature and deformation rate, the yield strength exhibits similar dependencies up to the point of brittle transition [43]. What is more, results that show potentially bimodal impact strength are sometimes not discussed—with the study focusing only on means (thereby implying unimodal structure)—for example in Kitao's [44] study on polyethylenes (notably with relevance to LLDPE in Fig. 3 and several cases in Fig. 4 of that work). The results that may point towards bimodality in that work may be found in the ductile-to-brittle transition region, typically nearer the brittle conditions. There, however, the lower and higher levels of the cases that may exhibit bimodality fall between the performances of the cases that clearly fall in the unimodal ductile or brittle modes.

In this work, bimodality is thought to originate in proximity to the ductile-to-brittle transition, in a similar way to that described by Sabbagh and Marchand [15] and—possibly—seen in some of Kitao's [44] results. In Viljoen et al. [11], it was found that the ductility (in terms of Young's modulus and elongation at break) of the composites in the present study was substantially reduced through the addition of CC. Based on this, it is theorised that the 30CC materials are near their ductile-to-brittle transition at room temperature, entering this bimodal region. This is motivated further by the presence of bimodality with and without CB and S in the 30CC materials, suggesting that this is not an effect related to only CB or S, although they play a role in the shifting proportions of high and low failures. The shifting proportions of high and low impact strength in this subset are accounted for by similar shifts in ductility, through the addition of SEBS (as part of the CB masterbatch) and S. The effects found in this work, with the loading of CB directly correlated to the probability of high impact strength and that of S inversely correlated to the same align with the findings of Viljoen et al. [11] in terms of elongation at break. This is consistent, as the notched edge of the impact specimen experiences a tensile loading due to the rotation of the sides of the tensile specimen around the edges of its holder, with fracture occurring once this

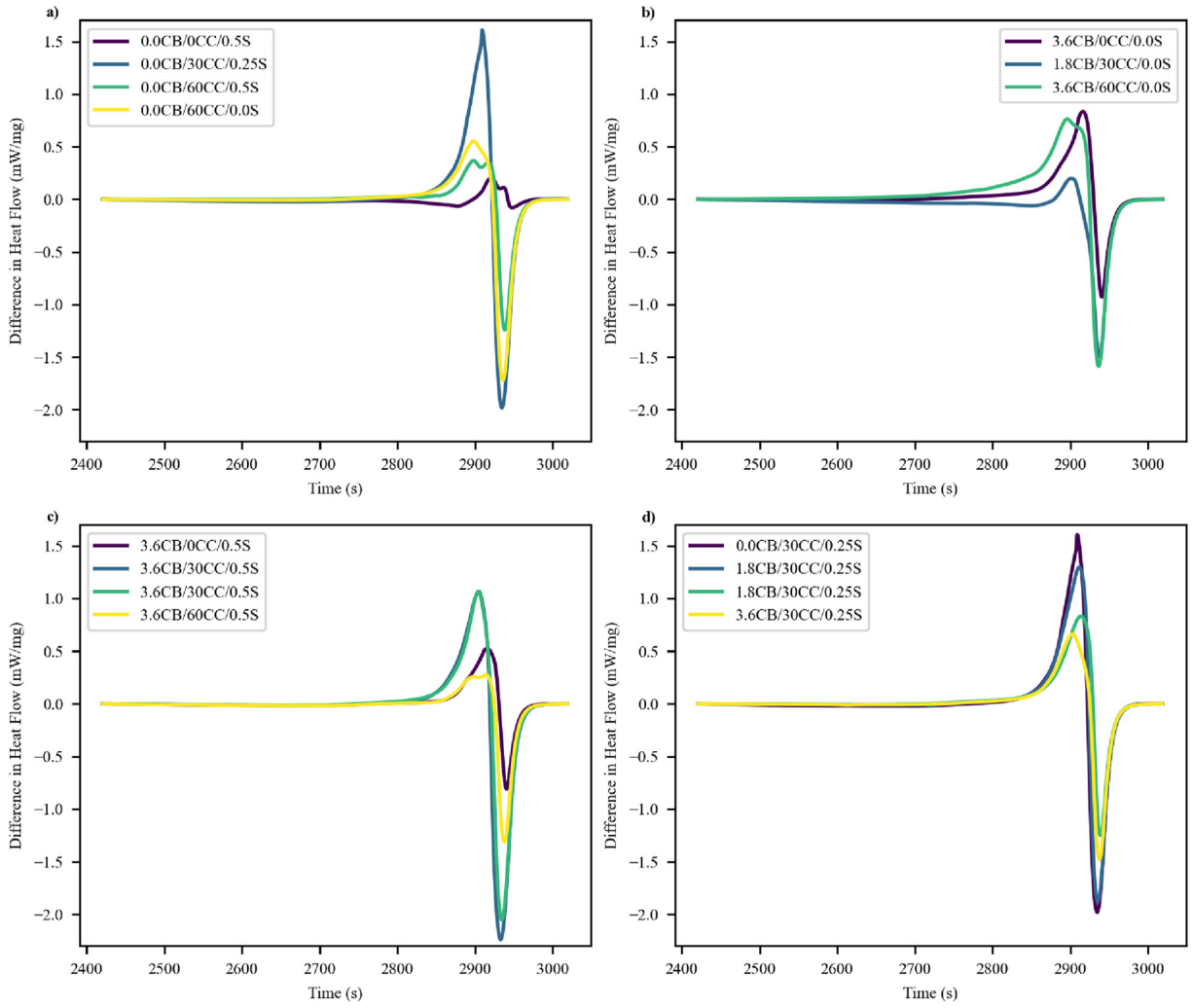


**Fig. 14.** Plot of the melting difference curves of a number of materials, highlighting (a) the effect of CC loading with no CB; (b) the effect of CC loading without S; (c) the effect of CC loading in 3.6CB/0.5S materials; and (d) the effect of CB loading in 30CC/0.25S materials.

loading (and accompanying strain) exceeds the capacity of the material.

The energy absorbed by a specimen during impact may be separated into that required for crack initiation and that for crack propagation [35]. Based on fractography, it would appear that the primary difference in the impact strength of the materials lies in their resistance to crack initiation, with evidence of far more energetic initiation present in the larger mirror zone of the stronger specimens. It is well established that faster crack propagations dissipate less energy, so it is likely that the weaker specimens dissipate more energy through propagation than the stronger specimens, owing to the slower fracture of the weaker specimens. This is also evidenced by the increased number of rib markings visible in these specimens.

The absence of clear evidence of bimodality in the unnotched specimens (in the 30CC materials) may be the result of the much-increased variance obfuscating the presence of two modes. However, it is likely that the behaviour for these specimens is shifted away from brittle fracture owing to the dependence of the ductile-to-brittle transition on specimen geometry, with brittle fracture much more likely in notched specimens [45].

Based on the evidence here presented, the authors believe the nearest approximation of the true behaviour could take the form of a model consisting of linear models for ductile (d), brittle (b) and very brittle (vb) failure modes, along with two logistic models and Bernoulli distributions with which to switch between these models according to Equation (8). This would allow for a three-way split, where notched impact strength results of greater than approximately 2 kJ/m$^2$ would be classified as ductile, those between 2 kJ/m$^2$ and 1.2 kJ/m$^2$ as brittle and those below 1.2 kJ/m$^2$ as very brittle. However, this approach could not be taken with the data at hand, as it would have required extrapolation (to support the ductile level in the 60CC materials, the very brittle level in the 30CC materials and the brittle and very brittle levels in the 0CC materials) and substantial changes to the model architecture to support the asymptotic behaviour that would then be found, certainly in the case of the ductile model. In addition, the available data would offer no information on the curvature of the ductile curve as a function of CC, likely resulting in a linear model—far from the expected asymptotic behaviour expected. For this model structure to be supported, additional levels of CC loading would be required, ideally with the existing levels of CB and S.

$$\hat{\mu}_{full} = \hat{\mu}_d(1 - \mathrm{B}(1, \hat{p}_b)) + \hat{\mu}_b \mathrm{B}(1, \hat{p}_b)(1 - \mathrm{B}(1, \hat{p}_{vb})) + \hat{\mu}_{vb} \mathrm{B}(1, \hat{p}_b)\mathrm{B}(1, \hat{p}_{vb}) \quad (8)$$

Nonetheless, the effects found using the models used are informative. These are summarised in Table 2 (pure-component effects) and Table 3 (interactive effects). Here, the rotation of the arrows is scaled based on the largest absolute value of an effect, between the primary and interactive effects, of a given measure. A distinction is made between insignificant (•) and null effects (–). It is compelling to note that the effects on the notched and unnotched impact strength mirror each other, keeping in mind the reduced data available to the model of the latter. More compelling still is the similarity between these effects and the effects on the likelihood of high or low impact strength, when considering that the expected true model discussed in the prior paragraph would see a direct correlation between CC loading and the degree of brittleness of a specimen. In general an increasing loading of CC results in reduced impact strength, which is sometimes seen in the case of a surface-treated ultra-fine material [46,47], likely due to insufficient compatibilisation of the CC resulting in premature debonding (likely as a result of weak interfacial interaction as well as particle agglomeration). This is in contrast with the more typical reinforcing effect, stemming from the formation of inter-particle ligaments of less than a certain critical thickness, that is frequently reported for fine and ultra-fine CC [40,48]. The positive squared effect for CC points towards the curvature of the system, emulating asymptotic curvature within the experimental range.

The effects of CB, predominantly as a result of the SEBS matrix of the masterbatch, are quite complex. SEBS tends to form a dispersed phase in HDPE and is typically seen to reduce impact strength [49,50]], passing through a trough—as seen in the 0CC specimens of this work. With sufficient compatibility, it may contribute to a toughening interlayer "bumper" around filler particles. This, however, would be clearly apparent from fractographs as such effects would substantially reduce the number of particles subject to clean debonding [49, 50]. In the (comparatively slow) tensile fracture [11] of specimens of the same formulations as those of the present work, extensive evidence of clean debonding was found under scanning electron microscopy. As a result, it is thought that the positive effects of CB in the CC-containing specimens stem from a slight decrease in ligament thickness [40,48] due to the addition of the SEBS dispersed phase. It is known that foreign compounds (such as SEBS and stabilisers in this case) are concentrated in the amorphous regions of HDPE owing to their structural incompatibility with the crystalline matrix [51–54]. The negative effects of the stabiliser package can likely be explained along similar lines. While the loadings of S are likely too low to meaningfully impact the crystallinity of the material [53, 54]], its molecules have substantially less chemical similarity to the matrix. It is likely, here, that the stabiliser package acts to reduce the number of tie molecules that are able to span the amorphous regions between crystalline regions; with these tie molecules associated with improved toughness in PE [55]. In addition, the stabiliser molecules may migrate to the surfaces of filler particles, as a result of increased chemical affinity [56,57], potentially further compromising the interactions between the matrix and the filler.

**Table 2**
Summary of pure-component formulation effects. nIS is divided based on high/low model effects.

| | CB | CC | S | $CB^2$ | $CC^2$ | $S^2$ |
|---|---|---|---|---|---|---|
| nIS | •/→ | ↓/↓ | →/→ | •/→ | ↗/↗ | •/→ |
| p (High) | ↗ | • | → | • | ↑ | → |
| uIS | ↗ | ↓ | → | N/A | N/A | N/A |

**Table 3**
Summary of interactive formulation effects. nIS is divided based on high/low model effects.

| | CBxCC | CBxS | CCxS |
|---|---|---|---|
| nIS | →/→ | →/• | —/• |
| p (High) | • | • | • |
| uIS | → | • | → |

The crystallinity results would suggest that substantial effects are present, owing to the approximately 20 % variation in HDPE crystallinity, but little beyond the obvious substitution effect with increasing CC is gained from the models. Based on the difference curves and the shifts in melting and crystallisation temperature, it is clear that the addition of additives results in increased nucleation, with increases in the proportion of smaller crystallites and decreases in the proportion of larger crystallites. With all else equal, this could be associated with increased impact strength as is seen with the addition of nucleating agents to polyolefins [7]. These effects are overridden by the additive-specific effects. For example, the peak in small-crystallite proportion around a CC loading of 30 % and no CB would, according to crystallinity alone, result in maximum toughness for this material. However, this is clearly not the case in the notched and unnotched cases.

## 5. Conclusions and recommendations

In this work, it was clearly demonstrated that bimodal impact strength may be encountered in notched specimens of HDPE composites of certain formulations. What is more, it was shown that the proportion of high- and low-impact-strength specimens is a function of formulation. The only prior literature to have shown this type of result found bimodality in PVC plaques, with shifts in proportion as a function of temperature. In the present work, as in the prior reported case, these effects are believed to be found in the vicinity of the ductile-to-brittle transition. Given the extent of the change in impact strength between the high and low levels, the authors believe it important for future works on impact strength to carefully consider the distribution of results where this may be the case, rather than basing analysis on a mere mean value to ensure adequate quality control and adherence to design specifications.

Clear evidence of bimodal behaviour is absent from unnotched specimens of the same formulations, which is likely results from the effects of notch geometry on the ductile-to-brittle transition of specimens.

Primary and interactive effects were studied using Bayesian analysis, with switching in the case of the notched specimens. The formulational effects outlined in Tables 2 and 3 were identified. A more comprehensive model, better reflecting what the authors expect to be the ground truth of the fracture behaviour was proposed for use in later studies with an increased number of experimental levels.

Covariance between the bulk morphology of materials, in terms of matrix crystallisation behaviour, and the impact strength of specimens was investigated, with no clear correlation found. Some formulational effects were found, however, on bulk crystallisation behaviour.

Further studies are needed to better understand the bimodal impact strength shown in this work. In particular, instrumented impact testing should prove valuable to better understand the distribution of impact energy between crack initiation and propagation and discern between different modes of crack propagation. This could be combined with high-speed photography to monitor

crack progression. Morphological work, such as that performed by Bartczak [48], may prove illuminating in terms of the origins of the bimodal behaviour, particularly in terms of the morphology around the filler particles and the interaction of the matrix with the elastomer and stabiliser system. Additional formulations in the ductile-to-brittle region should be investigated, with particular emphasis on calcium carbonate loading and its effects on the distribution of impact strengths, in an effort to better determine the number of failure modes and improve the ability for this behaviour to be modeled. Finally, the effects of notch geometry may offer insight into the generality of this phenomenon, and the degree of care with which these types of cases should be treated in production systems.

## Declaration of competing interest

The authors declare that they have no known competing financial interests or personal relationships that could have appeared to influence the work reported in this paper.

## Acknowledgements

The authors would like to thank their colleagues at the University of Pretoria and the Leibniz- Institut für Polymerforschung Dresden e. V. Particularly, they would like to thank Frieder Pursche and Christian Lehmann for their assistance in processing of the samples, Holger Scheibner for his assistance in mechanical characterisation, and Ivonne Hasselhorst for her assistance with FTIR spectroscopy. Further thanks are due to Omya of Oftringen, Switzerland, and Caparol Industrial Solutions of Grimma-Nerchau, Germany, for the materials that they provided. Funding: This work was supported by Techsparks (Pty) Ltd and the Technology and Human Resources for Industry Programme (THRIP), South Africa (grant number THRIP/133/March 31, 2016), administered by the Department of Trade, Industry and Competition, South Africa, for their contribution to a travel allowance for David Viljoen to visit the Leibniz-Institut für Polymerforschung Dresden e. V. David Viljoen is thankful to the Leibniz-Institut für Polymerforschung Dresden e. V. for the stipend he was provided during his stay.

## Appendix A. Supplementary data

Supplementary data to this article can be found online at https://doi.org/10.1016/j.aiepr.2023.11.001.

## References

[1] C.B. Bucknall, Toughened Plastics, Springer, 1977.
[2] Q. Fu, G. Wang, J. Shen, Polyethylene toughened by $CaCO_3$ particle: brittle-ductile transition of $CaCO_3$-toughened HDPE, J. Appl. Polym. Sci. 49 (4) (1993) 673–677.
[3] Q. Fu, G. Wang, Effect of morphology on brittle-ductile transition of HPDE/$CaCO_3$ blends, J. Appl. Polym. Sci. 49 (11) (1993) 1985–1988.
[4] M.A. Spalding, A. Chatterjee, Handbook of Industrial Polyethylene and Technology: Definitive Guide to Manufacturing, Properties, Processing, Applications and Markets Set, John Wiley & Sons, 2017.
[5] C. Vasile, M. Pascu, Practical Guide to Polyethylene, iSmithers Rapra Publishing, 2005.
[6] R. Koerner, Y. Hsuan, G. Koerner, Lifetime predictions of exposed geotextiles and geomembranes, Geosynth. Int. 24 (2) (2017) 198–212.
[7] M. Tolinski, Additives for Polyolefins: Getting the Most Out of Polypropylene, Polyethylene and TPO, William Andrew, 2015.
[8] Y.-L. Yang, S.-L. Bai, C. G'Sell, J.-M. Hiver, Mechanical properties and volume dilatation of HDPE/$CaCO_3$ blends with and without impact modifier, Polym. Eng. Sci. 46 (11) (2006) 1512–1522.
[9] G. Pircheraghi, A. Sarafpour, R. Rashedi, K. Afzali, M. Adibfar, Correlation between rheological and mechanical properties of black PE100 compounds-Effect of carbon black masterbatch, Express Polym. Lett. 11 (8) (2017).
[10] W.D. Viljoen, F.J.W.J. Labuschagne, The thermal stability of highly filled high-density polyethylene quaternary composites: interactive effects and improved measures, Polym. Test. 85 (2020) 106424.
[11] D. Viljoen, M. Fischer, I. Kühnert, J. Labuschagné, The tensile behaviour of highly filled high-density polyethylene quaternary composites: weld-line effects, DIC curiosities and shifted deformation mechanisms, Polymers 13 (4) (2021) 527.
[12] C.-J. Kim, C.R. Nelson, Has the US economy become more stable? A Bayesian approach based on a Markov-switching model of the business cycle, Rev. Econ. Stat. 81 (4) (1999) 608–616.
[13] P.D. Congdon, Applied Bayesian Hierarchical Methods, Chapman and Hall/CRC, 2010.
[14] J. Kruschke, Doing Bayesian Data Analysis: A Tutorial with R, JAGS, and Stan, 2014.
[15] A. Sabbagh, G. Marchand, Characterization of bimodal impact strength distribution in PVC using instrumented impact testing, in: ANTEC 2003 Conference Proceedings, 2003, pp. 3119–3122.
[16] ASTM D3418 – 15, Standard Test Method for Transition Temperatures and Enthalpies of Fusion and Crystallization of Polymers by Differential Scanning Calorimetry, Standard, ASTM International, Philadelphia, 2015.
[17] J. Salvatier, T.V. Wiecki, C. Fonnesbeck, Probabilistic programming in Python using PyMC3, PeerJ Computer Science 2 (2016) e55.
[18] M.D. Hoffman, A. Gelman, et al., The No-U-Turn sampler: adaptively setting path lengths in Hamiltonian Monte Carlo, J. Mach. Learn. Res. 15 (1) (2014) 1593–1623.
[19] A. Gelman, B. Goodrich, J. Gabry, A. Vehtari, R-Squared for Bayesian Regression Models, The American Statistician, 2019.
[20] J.K. Kruschke, Rejecting or accepting parameter values in Bayesian estimation, Advances in Methods and Practices in Psychological Science 1 (2) (2018) 270–280.
[21] J.A. Hartigan, P.M. Hartigan, The dip test of unimodality, Ann. Stat. (1985) 70–84.
[22] SAS Institute, SAS/STAT User's Guide: Version 6, vol. 2, SAS institute Incorporated, 1990.
[23] A. Siffer, P.-A. Fouque, A. Termier, C. Largouët, Are your data gathered?, in: Proceedings of the 24th ACM SIGKDD International Conference on Knowledge Discovery & Data Mining, 2018, pp. 2210–2218.
[24] Y.-J. Kang, Y. Noh, Development of Hartigan's dip statistic with bimodality coefficient to assess multimodality of distributions, Math. Probl Eng. 2019 (2019).
[25] A. Vehtari, A. Gelman, J. Gabry, Practical Bayesian model evaluation using leave-one-out cross-validation and WAIC, Stat. Comput. 27 (5) (2017) 1413–1432.
[26] S. Watanabe, A Widely Applicable Bayesian Information Criterion, 2012, p. 6338, arXiv preprint arXiv:1208.
[27] S. Watanabe, Information criteria and cross validation for Bayesian inference in regular and singular cases, Japanese Journal of Statistics and Data Science 4 (1) (2021) 1–19.
[28] M.A. Martínez-Beneito, D. Conesa, A. López-Quílez, A. López-Maside, Bayesian Markov switching models for the early detection of influenza epidemics, Stat. Med. 27 (22) (2008) 4455–4468.
[29] J.K. Kruschke, Bayesian analysis reporting guidelines, Nat. Human Behav. 5 (10) (2021) 1282–1291.
[30] A. Vehtari, A. Gelman, D. Simpson, B. Carpenter, P.-C. Bürkner, Rank-normalization, folding, and localization: an improved for assessing convergence of MCMC (with Discussion), Bayesian Analysis 16 (2) (2021) 667–718.
[31] M. Hayes, D. Edwards, A. Shah, Fractography in Failure Analysis of Polymers, William Andrew, 2015.
[32] S. Lampman, Fracture and fractography, in: Characterization and Failure Analysis of Plastics, ASM International, 2003.
[33] M. Böhning, U. Niebergall, A. Adam, W. Stark, Impact of biodiesel sorption on mechanical properties of polyethylene, Polym. Test. 34 (2014) 17–24.
[34] M. Böhning, U. Niebergall, A. Adam, W. Stark, Influence of biodiesel sorption on temperature-dependent impact properties of polyethylene, Polym. Test. 40 (2014) 133–142.
[35] M. Erdmann, U. Niebergall, V. Wachtendorf, M. Böhning, Evaluation of UV-induced embrittlement of PE-HD by Charpy impact test, J. Appl. Polym. Sci. 137 (36) (2020) 49069.
[36] M. Tanniru, R. Misra, On enhanced impact strength of calcium carbonate-reinforced high-density polyethylene composites, Mater. Sci. Eng., A 405 (1–2) (2005) 178–193.
[37] M. Tanniru, Q. Yuan, R. Misra, On significant retention of impact strength in clay–reinforced high-density polyethylene (HDPE) nanocomposites, Polymer 47 (6) (2006) 2133–2146.
[38] C. Deshmane, Q. Yuan, R. Misra, On the fracture characteristics of impact tested high density polyethylene–calcium carbonate nanocomposites, Mater. Sci. Eng., A 452 (2007) 592–601.
[39] J.L. González-Velázquez, Fractography and Failure Analysis, vol. 24, Springer, 2018.
[40] Z. Bartczak, A. Argon, R. Cohen, M. Weinberg, Toughness mechanism in semi-crystalline polymer blends: II. High-density polyethylene toughened with calcium carbonate filler particles, Polymer 40 (9) (1999) 2347–2365.
[41] E. Orowan, Fracture and strength of solids, Rep. Prog. Phys. 12 (1) (1949) 185.
[42] J. Sweeney, I.M. Ward, Mechanical Properties of Solid Polymers, John Wiley & Sons, 2012.
[43] I.M. Ward, J. Sweeney, Mechanical Properties of Solid Polymers, John Wiley & Sons, 2012.

[44] K. Kitao, A study of brittle-ductile transition in polyethylene, Polym. Eng. Sci. 37 (5) (1997) 777–788.
[45] G. Swallowe, Ductile-brittle transition, in: Mechanical Properties and Testing of Polymers, Springer, 1999, pp. 40–42.
[46] A. Lazzeri, S. Zebarjad, M. Pracella, K. Cavalier, R. Rosa, Filler toughening of plastics. Part 1–The effect of surface interactions on physico-mechanical properties and rheological behaviour of ultrafine $CaCO_3$/HDPE nanocomposites, Polymer 46 (3) (2005) 827–844.
[47] S. Sahebian, S.M. Zebarjad, S.A. Sajjadi, Z. Sherafat, A. Lazzeri, Effect of both uncoated and coated calcium carbonate on fracture toughness of HDPE/$CaCO_3$ nanocomposites, J. Appl. Polym. Sci. 104 (6) (2007) 3688–3694.
[48] Z. Bartczak, Mechanisms of toughness improvement of semi-crystalline polymers, J. Macromol. Sci., Part B 41 (4–6) (2002) 1205–1229.
[49] F. Sahnoune, J. Lopez-Cuesta, A. Crespy, Effect of elastomer interfacial agents on tensile and impact properties of $CaCO_3$ filled HDPE, J. Mater. Sci. 34 (3) (1999) 535–544.
[50] F. Sahnoune, J. Lopez Cuesta, A. Crespy, Improvement of the mechanical properties of an HDPE/PS blend by compatibilization and incorporation of $CaCO_3$, Polym. Eng. Sci. 43 (3) (2003) 647–660.
[51] A. Mokrini, M.A. Huneault, Z. Shi, Z. Xie, S. Holdcroft, Non-fluorinated proton-exchange membranes based on melt extruded SEBS/HDPE blends, J. Membr. Sci. 325 (2) (2008) 749–757.
[52] M. Šlouf, D. Michálková, V. Gajdošová, J. Dybal, J. Pilař, Prooxidant activity of phenolic stabilizers in polyolefins during accelerated photooxidation, Polym. Degrad. Stabil. 166 (2019) 307–324.
[53] H. Frank, Some oxidation characteristics of polypropylene, J. Polym. Sci., Polym. Symp. 57 (1976) 311–318. Wiley Online Library.
[54] N. Billingham, P. Calvert, I. Okopi, A. Uzuner, The solubility of stabilizing additives in polypropylene, Polym. Degrad. Stabil. 31 (1) (1991) 23–36.
[55] G. Tao, Y. Chen, J. Mu, L. Zhang, C. Ye, W. Li, Exploring the entangled state and molecular weight of UHMWPE on the microstructure and mechanical properties of HDPE/UHMWPE blends, J. Appl. Polym. Sci. 138 (30) (2021) 50741.
[56] X. Hu, H. Xu, Z. Zhang, Influence of fillers on the effectiveness of stabilizers, Polym. Degrad. Stabil. 43 (2) (1994) 225–228.
[57] C. Liauw, A. Childs, N. Allen, M. Edge, K. Franklin, D. Collopy, Effect of interactions between stabilisers and silica used for anti-blocking applications on UV and thermal stability of polyolefin film 1. Adsorption studies, Polym. Degrad. Stabil. 63 (3) (1999) 391–397.